Coastal Engineering 172 (2022) 104060

Contents lists available at ScienceDirect

Coastal Engineering

journal homepage: www.elsevier.com/locate/coastaleng

CFD investigation on scour beneath different configurations of piggyback pipelines under steady current flow

Vinicius Serta Fraga [a], Guang Yin [a,*], Muk Chen Ong [a], Dag Myrhaug [b]

[a] Department of Mechanical and Structural Engineering and Materials Science, University of Stavanger, Stavanger, Norway
[b] Department of Marine Technology, Norwegian University of Science and Technology, Trondheim, Norway

ARTICLE INFO

Keywords:
Scour
CFD
Piggyback pipelines
Steady current flow

ABSTRACT

Scour beneath piggyback pipelines laid on a sandy seabed is numerically investigated by solving two-dimensional (2D) Unsteady Reynolds-averaged Navier-Stokes (URANS) equations. The fluid flow and the sediment transport are resolved using a two-phase flow Eulerian-Eulerian numerical solver SedFoam based on the open-source code OpenFOAM. A parametric study is performed for different Shields parameters defined as $\theta = U_f^2/(s-1)gd_{50}$ of 0.068, 0.18 and 0.33 where U_f denotes the shear friction velocity on the seabed, the specific density of the sediment grains is $s = \rho^s/\rho^f$ where ρ^s and ρ^f are the density of the solid and fluid phases, respectively, g is the gravitational acceleration and d_{50} is the median grain diameter. Scour processes beneath piggyback pipelines under steady current flow condition are studied for different gap ratios of $G/D = 0, 0.15, 0.25$ and 0.35 between the main cylinder and the additional ones with a diameter ratio of $d/D = 0.3$ between them. Mesh convergence studies based on the scour depth and the sediment profile are performed to obtain an appropriate grid resolution. A validation study is performed by comparing the scour depth of the single cylinder cases with the published experimental results obtained by Mao (1986). The effects of different θ and geometry configurations on the scour depth and the sediment profile are obtained and discussed.

1. Introduction

The use of subsea pipelines for the transport of oil and gas is increasing as oil and gas fields are developed further offshore. To monitor the transport of oil in the pipeline, a new configuration of pipeline, called piggyback pipeline which comprises one large pipeline and a small one rigidly installed along with the main large pipeline, has been widely used for decades. The large pipe is usually used to transport the oil and gas and the small pipe can be used to transport the monitoring signal and the oil displacement material according to Jakobsen and Sayer (1995). By using the piggyback pipeline, the costs can be reduced during the installation phase by using a common route and allowing more than one product to be installed simultaneously. When the pipelines are placed on the seabed, strong currents may cause scour beneath the pipelines, which results in suspension of them. When the scour depth increases and extends along the pipelines, they may undergo vortex-induced vibrations (VIV), which may cause structure fatigue and reduce the life span of the pipelines. Therefore, the study of scour mechanisms beneath different configurations of pipelines is of great significance for engineering design.

Some experimental and numerical investigations were previous performed to analyze the scour beneath pipelines. Mao (1986) used experiments to study the scour beneath a stationary pipeline under steady current flow condition. It was concluded that the main scour process occurs in the jet region beneath the cylinder and in the wake region downstream of the cylinder. Besides, the scour develops faster in the early stages compared with the later ones and the final scour depth is less than the diameter of the cylinder. Sumer et al. (1988) carried out experimental investigations of a vibrating pipe exposed to current flow. The results were compared against those from fixed pipe and showed that after the occurrence of full vortex shedding the scour depth develops faster than the same for fixed pipes. Sumer and Fredsøe (1991) and Sumer et al. (2001) performed experimental studies of the onset of scour beneath a cylinder exposed to waves and currents, respectively. They found that the main mechanisms for the onset of scour were the increase of the pressure difference between the front and back faces of the pipes, which induces a seepage flow inside the sediment. This seepage flow will further reduce the submerged weight of sediments at

* Corresponding author.
E-mail address: guang.yin@uis.no (G. Yin).

https://doi.org/10.1016/j.coastaleng.2021.104060
Received 21 May 2021; Received in revised form 29 October 2021; Accepted 26 November 2021
Available online 29 November 2021

the downstream side of the pipes and a small gap will be formed beneath the pipes. When the local Shields parameter defined as $\theta = U_f^2/(s-1)gd_{50}$ is larger than 0.05, the movement of sediment is initiated and the large shear stress due to the high flow velocity within the gap will continuously cause the transport of the sediment beneath the pipes. The effects of seepage flow have also been extensively studied in Qi and Gao (2014), Guo et al. (2018) and Zhai et al. (2021a, b). The addition of spoilers attached to a pipeline was experimentally investigated by Chiew (1992). It was shown that the spoilers affect the scour process due to the increasing blockage of the flow the pipeline is subjected to. When the spoiler was attached to the upper part of the cylinder, an increase in the scour depth and in the lee-wake erosion was observed due to the highly deflected flow around the cylinder. However, the addition of the spoiler touching the soil resulted in no scour beneath the pipeline, which is explained by a reduction in the pressure gradient around the cylinder.

Apart from experiments, numerical simulations have also been used to study the scour phenomenon. Brørs (1999) investigated the scour process beneath a pipeline using the $k-\varepsilon$ turbulence model. The predicted results were in good agreement with previously published experimental data; however, the vortex shedding behind the pipeline was not captured by using the turbulence model. Zhu et al. (2013) performed numerical investigations of the scour beneath a submerged cylinder with a vertical spoiler attached on its top. The development of the scour occurs slightly faster as the spoiler height increases, which also contributes to the acceleration of the self-burial process. Zhao et al. (2016) employed a numerical model to study the scour beneath a pipeline subjected to steady currents. It was found that the standard $k-\varepsilon$ turbulence model was able to achieve accurate results predicting the local scour process. Lee et al. (2016) analyzed the application of a new two-phase model to predict the scour beneath a pipeline. The $k-\varepsilon$ turbulence model was employed, and a good agreement of the scour depth was obtained when compared to previous published experimental data reported by Mao (1986). On the other hand, the $k-\varepsilon$ turbulence model is not able to predict vortex shedding behind the pipeline, resulting in the underprediction of the lee-wake erosion downstream the cylinder. Larsen et al. (2016) performed numerical analysis of the scour beneath pipelines under currents and waves combined with the $k-\omega$ turbulence model. A good agreement was obtained when compared against previously published experimental data. Lasatira et al. (2017) carried out numerical investigation of the scour depth beneath two cylinders in tandem subjected to current flow. When the diameter of the upstream cylinder is larger than that of the downstream cylinder, the scour depth relative to the upstream cylinder decreases with the increasing gap between the pipelines. The opposite occurs when the upstream cylinder is larger than the downstream one, which reveals a significant dependency of the scour depth beneath the pipelines with the cylinder diameters and the gap between them. The scour beneath two pipelines in tandem subjected to waves and current was studied using numerical simulations by Li et al. (2019a). The $k-\omega$ turbulence model was employed with consistent results compared with published experimental data. It was shown that when the current governs the flow, a small gap between the two pipelines results in a single scour hole beneath them. It is also observed that the development of scour beneath the upstream pipeline occurs faster than the one beneath the downstream pipeline. Li et al. (2019b) investigated the effects of the upward seepage flow on the scour beneath a submarine pipeline. It was found that there is a positive correlation between the upward hydraulic gradient and the equilibrium scour width.

Due to the wide application of piggyback pipelines, their influences on scour have also been studied. It was reported that scour depths beneath piggyback pipelines are larger compared with that beneath a single pipeline. Moreover, the scour depth decreased with the increasing gap between the small and large pipelines as reported in Zhao and Cheng (2008) and Zhao et al. (2018). Mathieu et al. (2019) performed numerical simulations using a two-phase flow model to investigate the scour beneath a pipeline. The standard $k-\varepsilon$ and $k-\omega$2006 (Wilcox, 2006) turbulence models were compared based on the scour depth and the bed profile. The $k-\varepsilon$ model was able to capture accurately the scour depth beneath the pipeline; however, it was not able to predict vortex shedding behind the pipeline. On the other hand, the $k-\omega$2006 model was not able to predict well the scour depth beneath the pipeline while capable of resolving the vortex shedding behind the pipeline and consequently the lee-wake erosion downstream of the cylinder. It was found that the underestimation of the scour depth in the employed two-phase flow solver comes from the suppression of the negative contribution of the cross-diffusion term close to the interface between the sediment phase and the fluid phase when sediment transport is incorporated in the $k-\omega$2006 model. Overall, the $k-\varepsilon$ turbulence model can provide a good prediction of the scour depth development beneath the pipeline when compared to the published experimental data. Yang et al. (2019) carried out experimental and numerical analysis of the scour beneath different configurations of piggyback pipelines. They concluded that when an additional smaller cylinder is placed at the top of the main one, the scour depth increases. When two additional cylinders are placed attached to the main pipe and laid on the bed surface, the scour depth is significantly reduced compared with that beneath a single pipeline.

In the present study, scour simulations beneath piggyback pipelines with different configurations are performed employing a Eulerian-Eulerian two-phase flow solver SedFoam (Cheng et al., 2017) based on an open-source code OpenFOAM. This configuration is similar to that reported in Yang et al. (2019) and is considered to effectively reduce the scour depth. Two-dimensional (2D) Unsteady Reynolds-averaged Navier-Stokes (URANS) equations combined with the two-phase $k-\varepsilon$ and $k-\omega$2006 turbulence models are evaluated in the convergence and validation studies. The scour process under different Shields parameters $\theta = U_f^2/(s-1)gd_{50}$ larger than 0.05 is investigated, where U_f represents the shear friction velocity on the seabed, $s = \rho^s/\rho^f$ is the sediment to fluid density ratio where ρ^s and ρ^f are the density of the solid and fluid phases, respectively, g is the gravitational acceleration, and d_{50} is the median grain diameter. The diameter ratio between the cylinders is $d/D = 0.3$, where d is the diameter of the additional cylinders and D is the diameter of the main cylinder. In addition, effects of different gap ratios (G/D), where G is the distance between the additional cylinders and the main pipe, are analyzed. According to the authors' knowledge, there is currently limited discussion on the scour mechanism of this type of configurations.

The structure of the paper is organized as follows: the mathematical formulation and the numerical methods are given in Section 2. The computational overview, convergence studies and validation studies are presented in Section 3. The results and discussions are given in Section 4. Lastly, the main conclusions are presented in Section 5.

2. Mathematical formulation and numerical methods

2.1. Mathematical formulation

2.1.1. Governing equations

A Eulerian-Eulerian two-phase flow solver is employed in this study. Following the implementation used in Cheng et al. (2017) and Chauchat et al. (2017), the equations for mass conservation of the sediment and fluid phases can be described using the Einstein summation rule as:

$$\frac{\partial \varphi}{\partial t} + \frac{\partial \varphi u_i^s}{\partial x_i} = 0 \tag{1}$$

$$\frac{\partial (1-\varphi)}{\partial t} + \frac{\partial (1-\varphi) u_i^f}{\partial x_i} = 0 \tag{2}$$

where $i = 1, 2$ is the streamwise and the cross-stream directions and u_1, u_2 are the corresponding velocity components. The sediment fraction is

denoted as φ and the superscripts s and f represent the solid and fluid phases, respectively. Similarly, the momentum equations for the solid and fluid phases can be written as:

$$\frac{\partial \rho^s \varphi u_i^s}{\partial t}+\frac{\partial \rho^s \varphi u_i^s u_j^s}{\partial x_j}=-\varphi\frac{\partial P}{\partial x_i}-\frac{\partial P^s}{\partial x_i}+\frac{\partial \tau_{ij}^s}{\partial x_j}+\varphi\rho^s g+\varphi(1-\varphi)K\left(u_i^f-u_i^s\right) -(1-\varphi)\frac{1}{S_c}K\nu_t^f\frac{\partial \varphi}{\partial x_i} \tag{3}$$

$$\frac{\partial \rho^f (1-\varphi) u_i^f}{\partial t}+\frac{\partial \rho^f (1-\varphi) u_i^f u_j^f}{\partial x_j}=-(1-\varphi)\frac{\partial P}{\partial x_i}+\frac{\partial \tau_{ij}^f}{\partial x_j}+(1-\varphi)\rho^f g -\varphi(1-\varphi)K\left(u_i^f-u_i^s\right)+(1-\varphi)\frac{1}{S_c}K\nu_t^f\frac{\partial \varphi}{\partial x_i} \tag{4}$$

where the pressure is given by P, the density of the sediment and fluid phases is given by ρ^s and ρ^f, respectively, P^s is the normal stress of the sediment phase, τ_{ij}^s and τ_{ij}^f are the shear stress of the corresponding phases. Here τ_{ij}^f can be described as:

$$\tau_{ij}^f=\rho^f(1-\varphi)\left[2\nu_{\text{Eff}}S_{ij}^f-\frac{2}{3}k\delta_{ij}\right] \tag{5}$$

$$\nu_{\text{Eff}}=\nu_t^f+\nu_{\text{mix}} \tag{6}$$

$$S_{ij}^f=\frac{1}{2}\left(\frac{\partial u_i^f}{\partial x_j}+\frac{\partial u_j^f}{\partial x_i}\right)-\frac{1}{3}\left(\frac{\partial u_k^f}{\partial x_k}\right)\delta_{ij} \tag{7}$$

where ν_{Eff} is the effective viscosity, k is the turbulent kinetic energy, δ_{ij} is the Kronecker delta, and S_{ij}^f is the deviatoric term of the strain rate tensor for the fluid phase. The drag parameter K is expressed as:

$$K=0.75C_d\frac{\rho^s}{d}\left|\boldsymbol{u}^f-\boldsymbol{u}^s\right|(1-\varphi)^{h_{\text{exp}}} \tag{8}$$

$$C_d=\begin{cases}\dfrac{24}{Re_p}\left(1+0.15Re_p^{0.687}\right), & Re_p\le 1000,\\ 0.44, & Re_p>1000\end{cases} \tag{9}$$

$$Re_p=\frac{d}{\nu^f}(1-\varphi)\left|\boldsymbol{u}^f-\boldsymbol{u}^s\right| \tag{10}$$

where C_d represents the drag coefficient, d is the particle diameter, $h_{\text{exp}}=2.65$ is the hindrance exponent, Re_p is the particulate Reynolds number and ν^f is the kinematic viscosity of the fluid. The sediment shear stress τ_{ij}^s and normal stress p^s both consist of a collisional part and a frictional part as $\tau_{ij}^s=\tau_{ij}^{sf}+\tau_{ij}^{sc}$ and $p^s=p^{sf}+p^{sc}$. In the current study, the granular stress model employed is the kinetic theory for granular flows to resolve the collisional part of τ_{ij}^{sc} and p^{sc}, which was originally developed by Ding and Gidaspow (1990). The detailed information of the kinetic theory can be found in Cheng et al. (2017) and Mathieu et al. (2019).

For the frictional part, the normal stress due to the permanent contact pressure can be calculated by:

$$p^{sf}=\begin{cases}Fr\dfrac{(\varphi-\varphi_{\min}^{\text{Fric}})^{\eta_0}}{(\varphi_{\max}-\varphi)^{\eta_1}}, & \varphi\ge\varphi_{\min}^{\text{Fric}},\\ 0, & \varphi<\varphi_{\min}^{\text{Fric}}\end{cases} \tag{11}$$

where $Fr=0.05$, $\eta_0=3$ and $\eta_1=5$. The value of $\varphi_{\min}^{\text{Fric}}=0.57$ is used corresponding to a random loose packing concentration of the sediment and $\varphi_{\max}=0.635$ is used as the maximum value of the sediment concentration and when $\varphi=0$, the computational cell is fully occupied with the fluid phase. The frictional shear stress τ_{ij}^{sf} is given by $2\mu^{sf}S_{ij}^s$ where S_{ij}^s is the sediment shear rate and μ^{sf} is the frictional viscosity calculated by $\mu^{sf}=\sqrt{2}p^{sf}\sin(\theta_f)/2\sqrt{S_{ij}^sS_{ij}^s}$. The angle of repose $\theta_f=32^o$ is used for the sediment in the present study.

2.1.2. Turbulence modeling

Two different URANS turbulence models are evaluated for the two-phase flow simulations, the two-phase $k-\varepsilon$ model (Cheng and Hsu, 2014; Cheng et al., 2017; Chauchat et al., 2017) and the two-phase $k-\omega$2006 model (Chauchat et al., 2017; Nagel et al., 2020) adapted from the Wilcox (2006) and Wilcox (2008) reformulated $k-\omega$ model. The general transport equation of k is given by:

$$\frac{\partial k}{\partial t}+u_j^f\frac{\partial k}{x_j}=\frac{R_{ij}^f}{\rho^f}\frac{\partial u_i^f}{\partial x_j}-\beta^*k\omega+\frac{\partial}{\partial x_j}\left[\left(\nu^f+\sigma_k\nu_t^f\right)\frac{\partial k}{\partial x_j}\right]-\frac{2K(1-\alpha)\varphi k}{\rho^f} -\frac{\nu_t^f}{S_c(1-\varphi)}\frac{\partial \varphi}{\partial x_j}(s-1)g \tag{12}$$

where R_{ij}^f is the Reynolds stress tensor.

The general transport equation of the two-phase energy dissipation rate ε can be written as:

$$\frac{\partial \varepsilon}{\partial t}+u_j^f\frac{\partial \varepsilon}{x_j}=C_{1\varepsilon}\frac{\varepsilon}{k}\frac{R_{ij}^f}{\rho^f}\frac{\partial u_i^f}{\partial x_j}+\frac{\partial}{\partial x_j}\left[\left(\nu^f+\sigma_\varepsilon\nu_t^f\right)\frac{\partial \varepsilon}{\partial x_j}\right]-C_{2\varepsilon}\frac{\varepsilon^2}{k}-C_{3\varepsilon}\frac{2K(1-\alpha)\varphi\varepsilon}{\rho^f} -C_{4\varepsilon}\frac{\varepsilon}{k}\frac{\nu_t^f}{S_c(1-\varphi)}\frac{\partial \varphi}{\partial x_j}(s-1)g \tag{13}$$

$$\nu_t^f=\beta^*\frac{k^2}{\varepsilon} \tag{14}$$

where ν_t^f is the turbulent viscosity employed in the two-phase $k-\varepsilon$ model and the constants of the model are: $\beta^*=0.09$, $\sigma_k=1$, $\sigma_\varepsilon=0.77$, $C_{1\varepsilon}=1.44$, $C_{2\varepsilon}=1.92$, $C_{3\varepsilon}=1.2$ and $C_{4\varepsilon}=1$.

The general transport equation of the two-phase specific dissipation rate ω can be described as:

$$\frac{\partial \omega}{\partial t}+u_j^f\frac{\partial \omega}{x_j}=C_{1\omega}\frac{\omega}{k}\frac{R_{ij}^f}{\rho^f}\frac{\partial u_i^f}{\partial x_j}+\frac{\partial}{\partial x_j}\left[\left(\nu^f+\sigma_\omega\nu_t^f\right)\frac{\partial \omega}{\partial x_j}\right]-C_{2\omega}\omega^2 -C_{3\omega}\frac{2K(1-\alpha)\varphi\omega}{\rho^f}-C_{4\omega}\frac{\omega}{k}\frac{\nu_t^f}{S_c(1-\varphi)}\frac{\partial \varphi}{\partial x_j}(s-1)g_j+\sigma_d\frac{1}{\omega}\frac{\partial k}{x_j}\frac{\partial \omega}{x_j} \tag{15}$$

$$\nu_t^f=\frac{k}{max\left[\omega, C_{\text{lim}}\dfrac{S_{ij}^f}{\sqrt{\beta^*}}\right]} \tag{16}$$

$$\sigma_d=\begin{cases}\dfrac{1}{8}, & \dfrac{\partial k}{x_j}\dfrac{\partial \omega}{x_j}\ge 0,\\ 0, & \dfrac{\partial k}{x_j}\dfrac{\partial \omega}{x_j}<0\end{cases} \tag{17}$$

where the cross-diffusion term is given by $\frac{\partial k}{x_j}\frac{\partial \omega}{x_j}$. The model constants employed in the two-phase $k-\omega$2006 model are: $\sigma_k=0.6$, $\sigma_\omega=0.5$, $C_{1\omega}=0.52$, $C_{2\omega}=0.0708$, $C_{3\omega}=0.35$, $C_{4\omega}=1$ and $C_{lim}=0.875$.

2.2. Numerical methods

The present investigations are performed in the open-source Computational Fluid Dynamics (CFD) toolbox OpenFOAM. A two phase-flow model first implemented by Cheng et al. (2017) and Chauchat et al. (2017) is used in all the sediment transport simulations. The PIMPLE algorithm is employed, which is a combination of the Semi-Implicit Method for Pressure-Linked Equations (SIMPLE) and Pressure-Implicit with Splitting of Operator (PISO) algorithms. Gauss linear is applied for divergence and gradient schemes, while the Laplacian schemes use Gauss linear corrected.

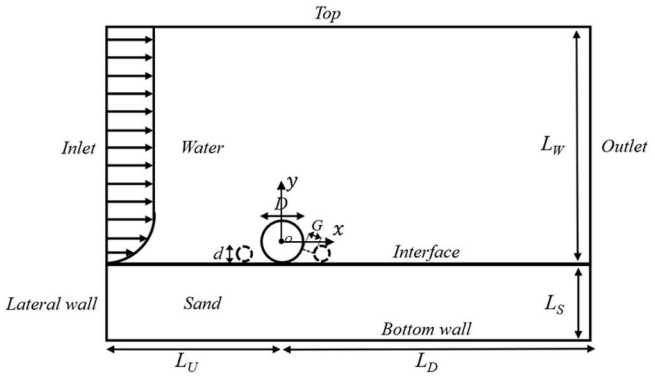

Fig. 1. Computational domain and boundary conditions.

Table 1
Corresponding U_f, undisturbed streamwise velocity at the top of the cylinder level and Re for each Shields parameter for the single cylinder cases.

θ	$U_f(m/s)$	$u_{top}(m/s)$	Re
0.068	0.0196	0.42	21000
0.18	0.0319	0.58	29000
0.25	0.0376	0.68	34000
0.33	0.0432	0.78	39000
0.43	0.0493	0.90	45000

3. Computational overview, convergence and validation studies

3.1. Computational overview

The computational domain is presented in Fig. 1. Cases with a single pipeline and piggyback pipelines are investigated. In all cases, the pipelines are stationary and initially mounted on the sediment layer without embedment. The diameter of the main pipe is $D = 0.05$ m and the specific density of the sediment grains is $s = 2.6$, similar to quartz sand. In the parametric study, different gap ratios of $G/D = 0$, 0.15, 0.25 and 0.35 and Shields parameter of $\theta = 0.068$, 0.18 and 0.33 are investigated. The corresponding U_f, the undisturbed velocity at the top of the cylinder level u_{top} and the Reynolds number ($Re = u_{top}D/\nu^f$) for all θ with the single cylinder cases employed in the current work are given in Table 1.

The height of the initial water phase is $L_W = 4.6D$, while the height of the initial sediment phase is $L_S = 2D$. The upstream length from the inlet to the center of the main cylinder is $L_U = 15D$ and the downstream length from the center of the main pipe to the outlet is $L_D = 30D$. Overall, the domain dimensions are similar to those used by Lee et al. (2016) and Mathieu et al. (2019). Compared with these previously published studies where $L_D = 20D$ and $L_S = 1.5D$, the downstream length L_D is increased to ensure the absence of far-field effects and the initial sediment height L_S is also increased to ensure that the scour depth is not affected by the bottom wall. The boundary conditions are the same as used in Mathieu et al. (2019):

(i) The top boundary is set as a symmetry plane for the velocities and pressure.
(ii) At the inlet, a log profile is used for the streamwise velocity, and the cross-stream component is equal to zero from the sediment layer at $y = 0$ to $y = L_W$ given as

$$u(y) = \frac{U_f}{\kappa}\ln\left(\frac{30y}{k_s}\right) \tag{18}$$

$$v(y) = 0 \tag{19}$$

where the von Kármán constant is $\kappa = 0.41$ and Nikuradse's equivalent sand roughness is $k_s = 2.5d_{50}$ with $d_{50} = 0.00036$ m, corresponding to medium sand (Soulsby, 1997). The value of U_f is determined according to the value of θ. From the bottom at $y = -L_S$ to $y = 0$, the velocities are set to be zero. The pressure is set as zero gradient at the inlet.

(iii) At the bottom wall and on the cylinders' surfaces, the velocities are zero and the pressure is set as zero gradient. Wall functions are applied on the cylinder surfaces and $y^+ \approx 30$ is satisfied with y^+ defined as:

$$y^+ = \frac{U_f \Delta y}{\nu} \tag{20}$$

where the center of the first grid size away from the cylinder is given by Δy.

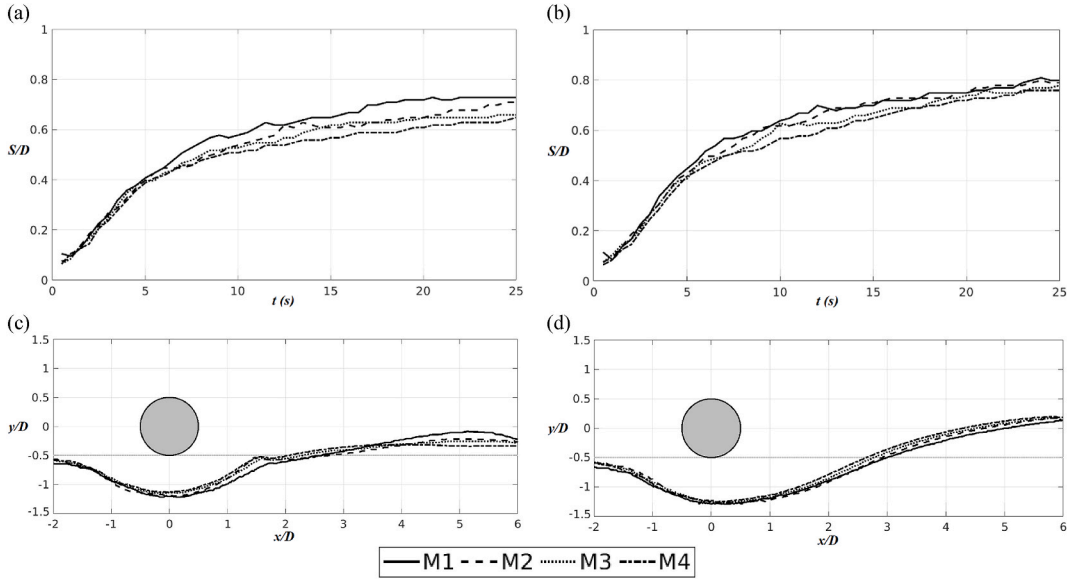

Fig. 2. Grid resolution study based on the scour depth for (a) $k-\omega$2006 and (b) $k-\varepsilon$ turbulence models, and bed profile for (c) $k-\omega$2006 and (d) $k-\varepsilon$ turbulence models.

Table 2
Results for the cases with $B/D = 0$ based on different numbers of grids.

Mesh	No. of elements	Max. S/D $k-\omega$2006	Max. S/D $k-\varepsilon$	BSS Profile $k-\omega$2006	BSS Profile $k-\varepsilon$
M1	81209	0.728	0.809	–	–
M2	109261	0.708	0.799	0.9561	0.9823
M3	139074	0.658	0.779	0.9848	0.9897
M4	182574	0.648	0.759	0.9669	0.9874

(iv) At the outlet, the velocities are set as zero gradient for the outgoing flow and set as zero for the incoming flow, respectively. The reduced pressure is set as $p = \rho^f gy$.

3.2. Convergence studies

A mesh convergence study is performed to evaluate the grid resolution for both $k-\varepsilon$ and $k-\omega$2006 turbulence models. Four different grid sizes (M1, M2, M3, M4) for the single cylinder case with $\theta = 0.33$ are analyzed with a minimum increment of 30% in the number of grid cells. This Shields parameter of $\theta = 0.33$ is chosen according to the benchmark experimental studies reported by Mao (1986). The time histories of the scour depth (S/D) beneath the cylinder and the sediment

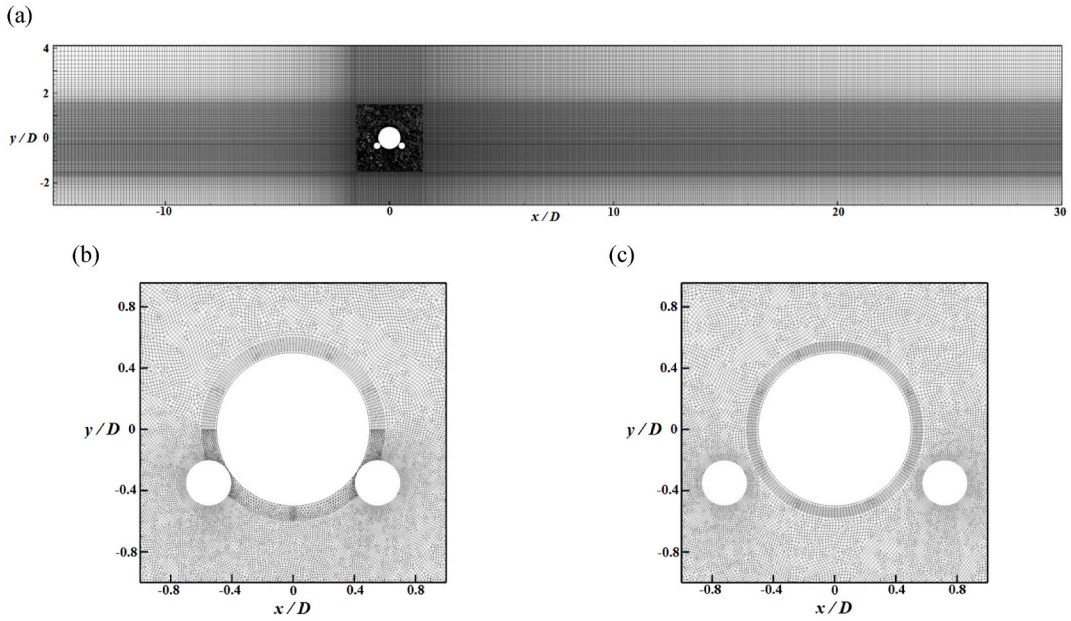

Fig. 3. The computational mesh of the (a) entire domain of the $G/D = 0$ case, (b) close view of the $G/D = 0$ case and (c) close view of the $G/\ D = 0.15$ case.

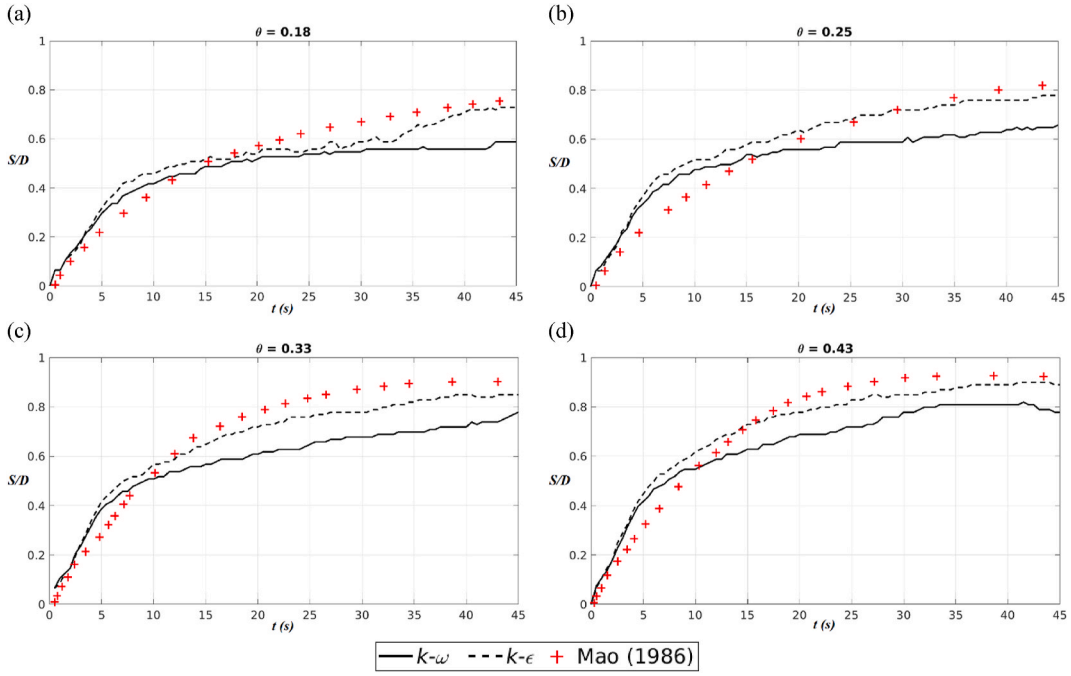

Fig. 4. Time-history of the scour depth compared to the experimental data for (a) $\theta = 0.18$, (b) $\theta = 0.25$, (c) $\theta = 0.33$ and (d) $\theta = 0.43$

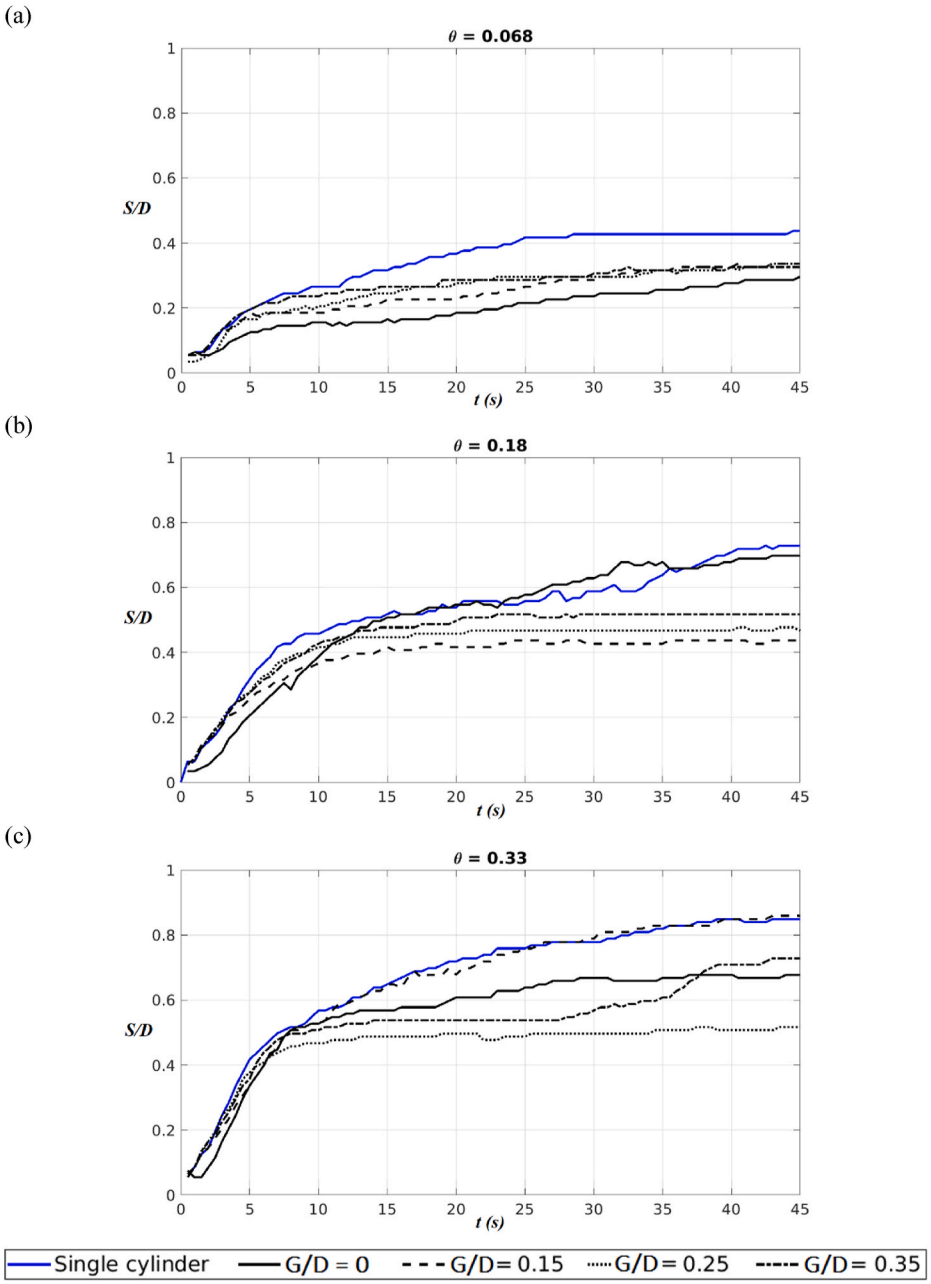

Fig. 5. Time-history of the scour depth for different geometry configurations and (a) $\theta = 0.068$, (b) $\theta = 0.18$, (c) $\theta = 0.33$

profiles denoted as $\varphi = 0.5$ according to Mathieu et al. (2019) at 25 s for different grid resolutions are given in Fig. 2. A reasonable convergence is obtained for the evolution of the scour depth. A good convergence for the bed profile is also achieved beneath the pipeline and in wake flow region behind the pipeline. Furthermore, the quantitative results are presented in Table 2. The maximum scour depth is compared for different grid resolutions and a good convergence is obtained with relative differences around 2% between the two most refined grids for both turbulence models. The bed profiles are evaluated in the spanwise range of $-2D$ to $6D$ employing the Brier Skill Score (BSS) statistical tool according to Mathieu et al. (2019). The BSS expression can be described as:

$$BSS = 1 - \frac{\sum_i^n \left(y_i^b - y_i^a\right)^2}{\sum_i^n \left(y_i^0 - y_i^a\right)^2} \tag{21}$$

where y^0 is the initial bed profile height, y^b represents the height of the bed profile for the analyzed grid resolution, and y^a denotes the bed profile height for the previous coarser mesh. If the value of BSS is equal to one, a perfect agreement is achieved. High values of $BSS \geq 0.96$ are obtained for both $k-\varepsilon$ and $k-\omega$2006 models, which indicates that the different grid sizes are able to capture similar behaviors of the flow, resulting in bed profiles with negligible differences. Therefore, an overall good grid convergence has been obtained and the finest mesh M4 is used for the validation and parametric studies. Similar grid resolutions especially around the pipelines and near the sediment surface as the mesh M4 are used for the piggyback pipelines cases and example meshes with different values of G/D are displayed in Fig. 3.

3.3. Validation studies

The time history of the scour depth of the single cylinder case is validated against the experimental data obtained by Mao (1986). Different Shields parameters of $\theta = 0.18$, 0.25, 0.33 and 0.43 are

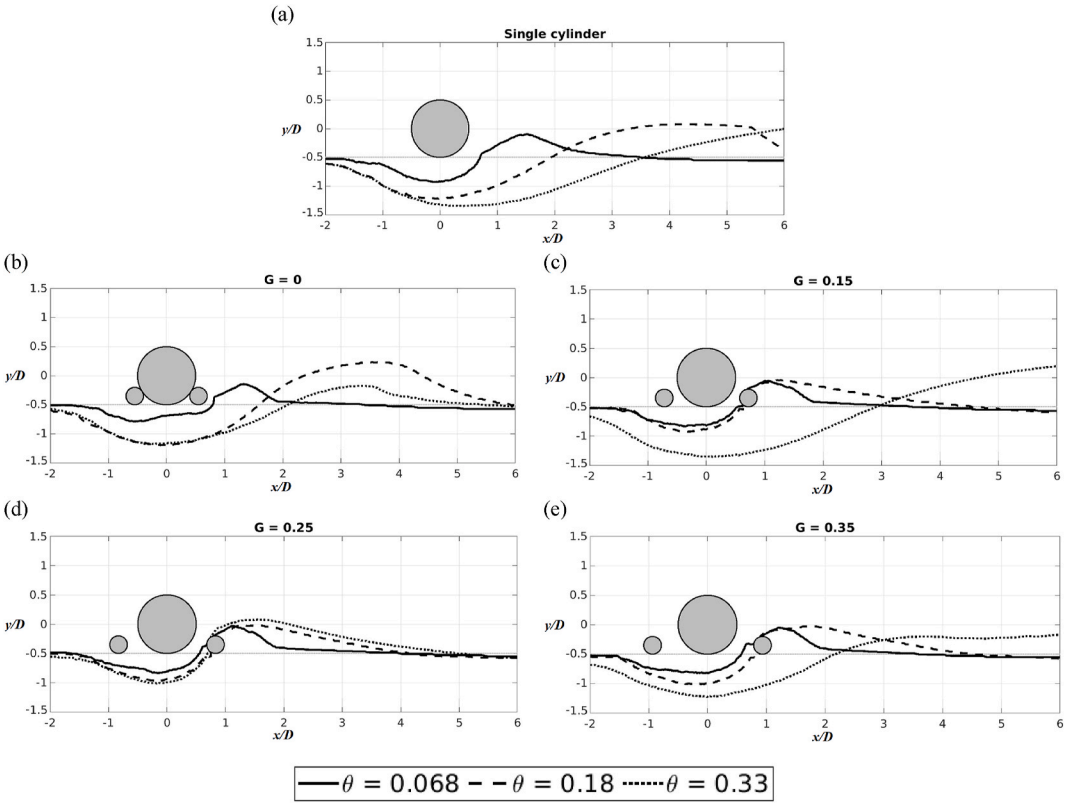

Fig. 6. Bed profile at 45 s for different Shields parameters and different geometries: (a) single cylinder, (b) $G/D = 0$, (c) $G/D = 0.15$, (d) $G/D = 0.25$ and (e) $G/D = 0.35$

analyzed and both the $k-\varepsilon$ and $k-\omega$2006 turbulence models are evaluated. Fig. 4 clearly shows a better agreement when the $k-\varepsilon$ turbulence model is used compared with the $k-\omega$2006 turbulence model which results in a significant underprediction of the scour depth by the latter model due to the suppression of the negative cross-diffusion term close to the interface between the sediment and fluid phases. This is in accordance with the results obtained by Mathieu et al. (2019). It should be noted that the negative cross-diffusion term is a specific feature when the $k-\omega$2006 is modified and implemented in the two-phase flow solver, which does not appear in the single-phase flow model adopted in Larsen et al. (2016) and Li et al. (2019a). Overall, the results from the scour depth are in good agreement when $k-\varepsilon$ model is used, which demonstrates good capabilities in resolving and predicting the scour in the gap flow region beneath the pipeline and predicting the scour hole development beneath the pipeline. Thus, the $k-\varepsilon$ turbulence model is used for all the simulations of scour beneath piggyback pipelines in the present study.

4. Results and discussion

4.1. Scour depth and bed profile

The time histories of the scour depth beneath the pipelines for all the geometry configurations based on different θ is shown in Fig. 5. As observed by Mao (1986) and Yang et al. (2019), the rate of the scour development beneath the cylinders is higher in the early stages compared with the later time steps of $t > 10s$. In general, the additional smaller cylinders lead to a reduction in the maximum scour depth compared with the single cylinder case which is in accordance with the observations reported by Yang et al. (2019). Moreover, higher values of θ tend to result in larger values of S/D. The single cylinder cases resulted in the highest scour depths for $\theta = 0.068$ and $\theta = 0.18$, while a similar depth in the single cylinder and the $G/D = 0.15$ configurations was obtained for $\theta = 0.33$. For the piggyback pipelines, the critical G/D among the investigated value, which results in the minimum scour depth, tends to be larger as θ increases; i.e. $G/D = 0$, $G/D = 0.15$ and $G/D = 0.25$ for $\theta = 0.068$, $\theta = 0.18$ and $\theta = 0.33$, respectively.

The bed profiles for the different geometries at 45 s are given in Fig. 6. The incapacity of resolving vortex shedding behind the pipeline

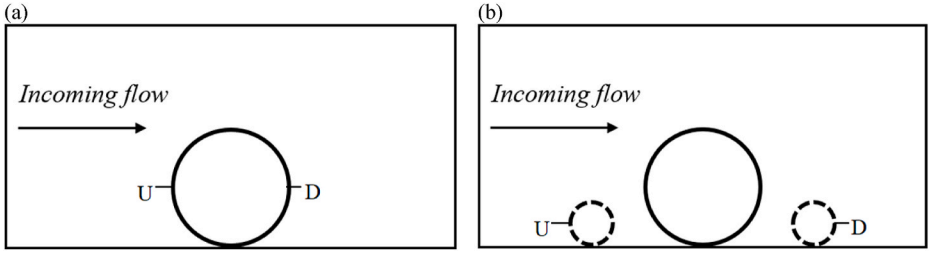

Fig. 7. Upstream and downstream positions where the pressure is obtained for (a) single cylinder cases and (b) piggyback configurations.

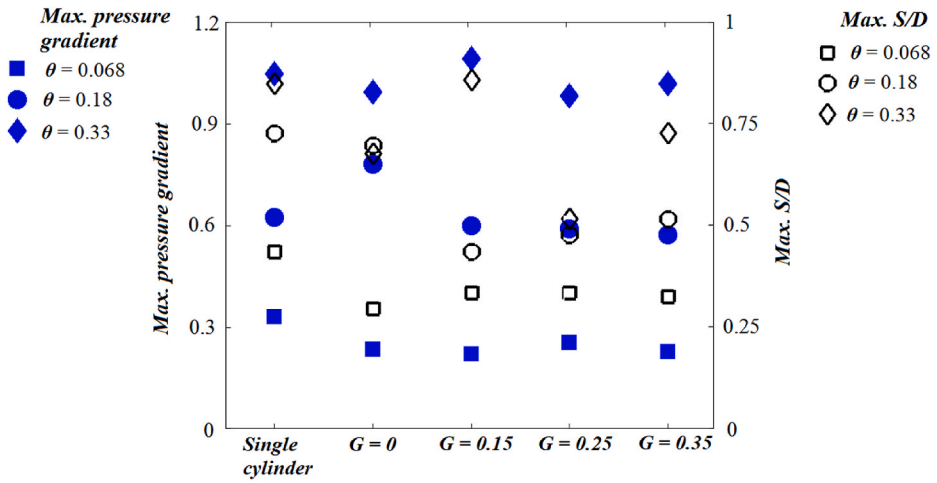

Fig. 8. Highest pressure difference and maximum scour depth for different Shields parameters and geometries.

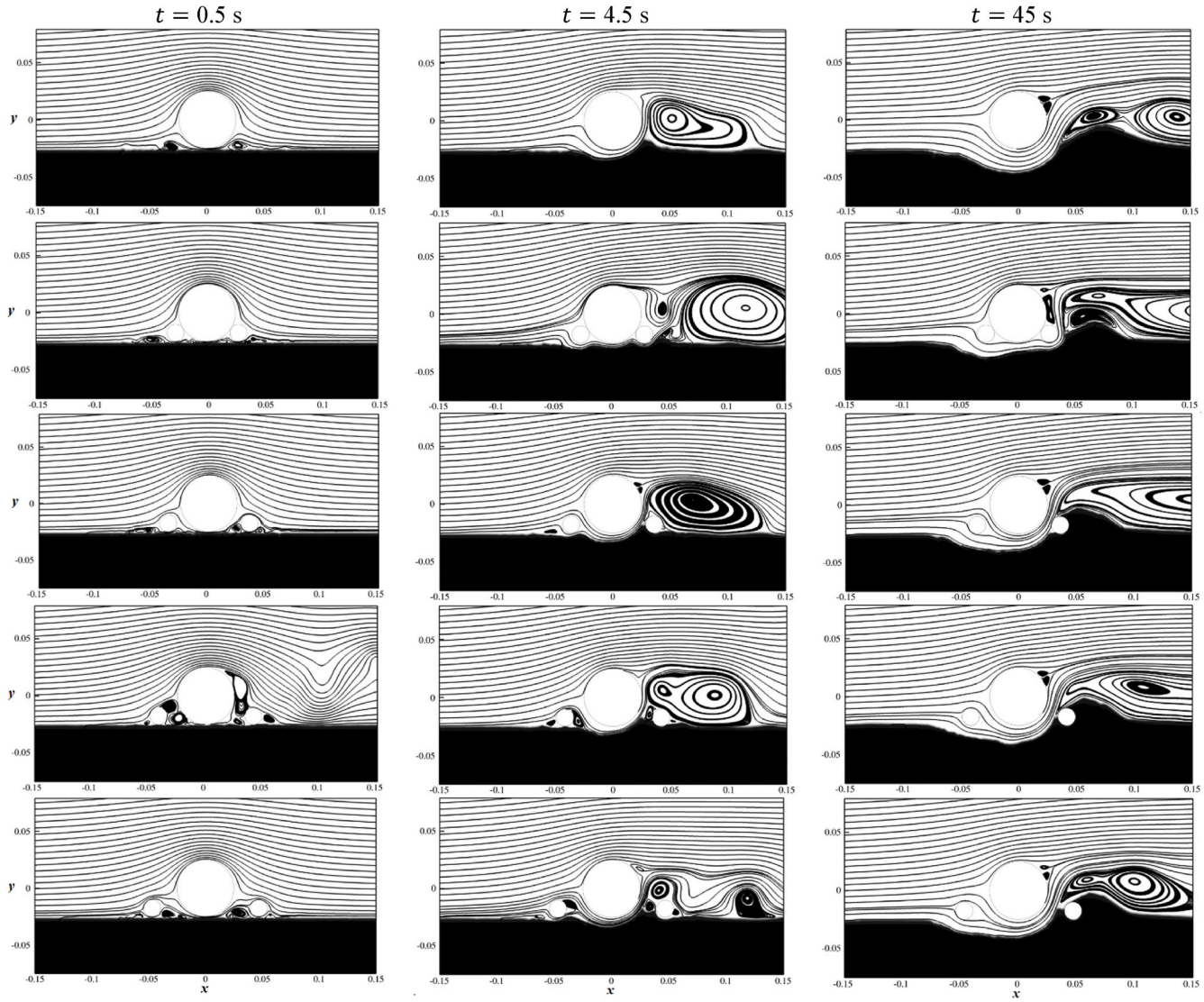

Fig. 9. The streamlines for $\theta = 0.068$ of the (upper) single cylinder case and the piggyback pipelines with increasing G/D from the upper to the lower rows at (left) $t = 0.5$ s, (middle) $t = 4.5$ s and (right) $t = 45$ s.

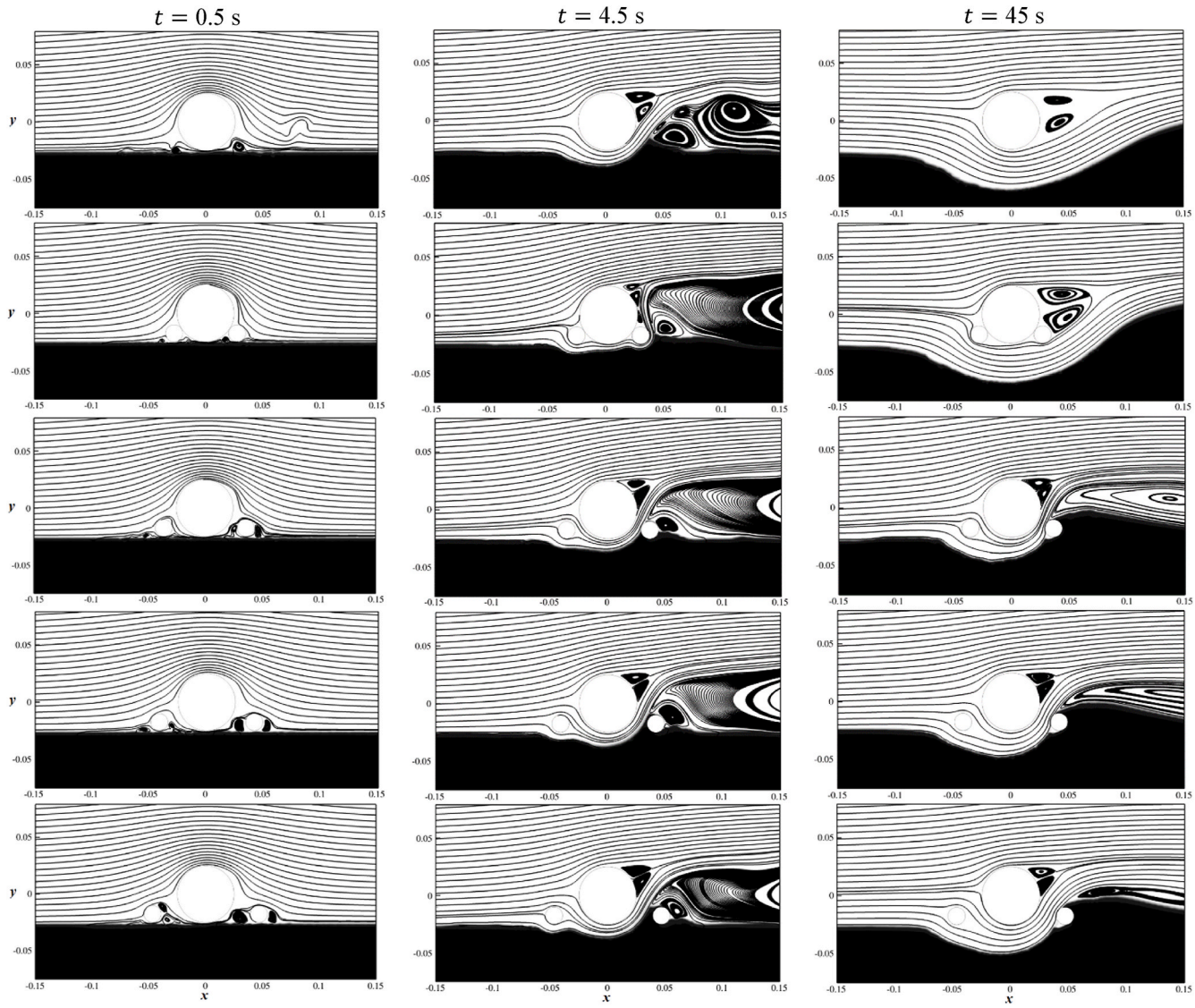

Fig. 10. The streamlines for $\theta = 0.18$ of the (upper) single cylinder case and the piggyback pipelines with increasing G/D from the upper to the lower rows at (left) $t = 0.5$ s, (middle) $t = 4.5$ s and (right) $t = 45$ s.

by using the $k - \varepsilon$ turbulence model and consequently the lee-wake erosion downstream the cylinders leads to a build-up of sediment far downstream the back face of the main cylinder. However, it does not seem to have any significant impact in the scour depth beneath the cylinders as also noted by Lee et al. (2016) and Mathieu et al. (2019). The sand dunes tend to concentrate closer to the pipeline for lower values of θ, which demonstrates the lower capacity of weak shear flow on the sediment surface to carry significant amounts of sediment compared with strong shear flow with higher θ. As observed in Fig. 5, the scour depth beneath the pipelines tends to be larger as θ increases for all the geometries. Moreover, the accumulation of sediments over the back face of the downstream cylinders indicates small scour depths as seen in Fig. 6 (c), (d) and (e). Furthermore, for all the configurations it is observed that the lower the scour depth is, the closer is the location of the maximum height of the dune to the pipeline.

4.2. Pressure gradient and vorticity

To understand the influence of θ and G/D on S/D, the pressure gradients and the streamlines around the pipelines for different cases are discussed in the current section. The pressure gradient $\partial(p/\gamma)/\partial x$ between the front and back faces of the main cylinder for the single cylinder cases and the two faces of the two additional cylinders as indicated in Fig. 7 is computed according to Sumer et al. (2001):

$$\frac{\partial\left(\frac{p}{\gamma}\right)}{\partial x} \approx \frac{p_U - p_D}{\gamma \overline{UD}} \tag{22}$$

where $\gamma = \rho^f g$ is the specific weight of water and the subscripts U and D denote the upstream and downstream positions where the pressure is taken, respectively.

Fig. 8 displays the highest $\partial(p/\gamma)/\partial x$ for the scour process and the maximum S/D at 45s. In general, for the single cylinder and the G/D cases, increasing the values of θ results in significant high pressure gradients for the investigated values of G/D. Furthermore, the piggyback configurations generally lead to lower pressure gradients and consequently lower S/D compared with those for the single cylinder cases, except for $\theta = 0.33$ with $G/D = 0.15$. The tendency of the pressure difference reduction may be explained by the shielding effect originated from the addition of the smaller cylinders, as found in Yang et al. (2019). For the same θ, the variations of pressure gradient with G/D are small. This suggests that the pressure difference is mainly driven by θ and has a significant effect on the final S/D as noted by Mao (1986), Sumer and

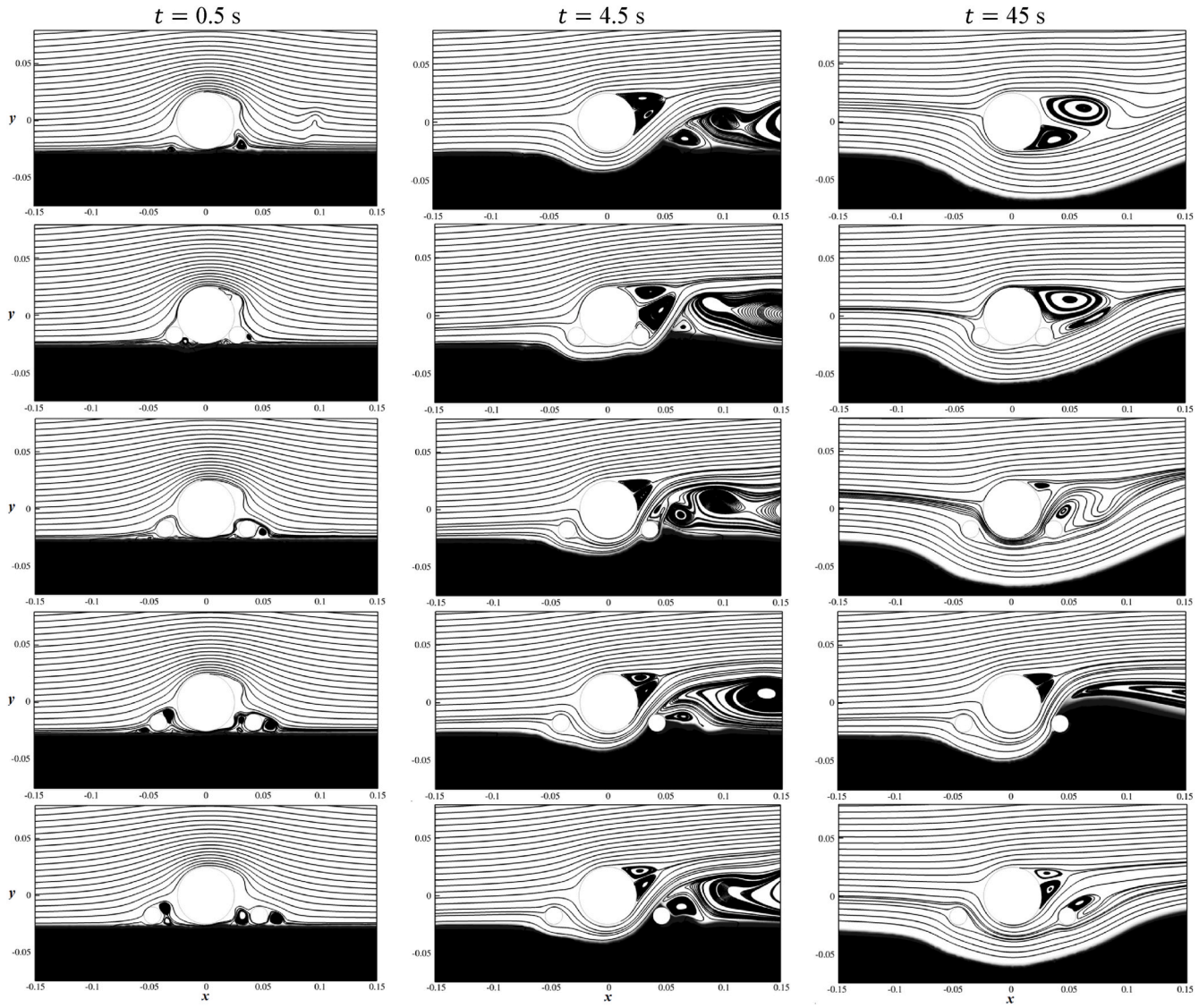

Fig. 11. The streamlines for $\theta = 0.33$ of the (upper) single cylinder case and the piggyback pipelines with increasing G/D from the upper to the lower rows at (left) $t = 0.5$ s, (middle) $t = 4.5$ s and (right) $t = 45$ s.

Fredsøe (1991) and Sumer et al. (2001). However, it is not the dominant mechanism that determines the final S/D for all the investigated cases. This will be elaborated further subsequently.

Figs. 9–11 illustrate the streamlines of the flow at different time instances: $t = 0.5$ s, immediately after the onset of scour beneath the cylinders, $t = 4.5$ s, when the pressure gradient is highest for the scour process for most of the cases, and $t = 45$ s corresponding to the equilibrium situation. The results for $\theta = 0.068$ are given in Fig. 9 showing that the presence of additional cylinders at $G/D = 0$ and 0.15 contributes to reduce the size of vortices attached upstream and downstream of the main cylinder at the bed level at $t = 0.5$ s. As G/D increases, these vortices are able to emerge. For the single cylinder case, the absence of any obstacle downstream of the main pipeline allows a strong recirculation motion to develop attached to the back face of the cylinder at $t = 4.5$ s. In the piggyback cases the center of this strong vorticity is shifted downstream, resulting in lower scour developments beneath the cylinders. Moreover, the gap flow beneath the piggyback is not strong enough to create a tunnel beneath the entire pipelines for $G/D = 0.15$, 0.25 and 0.35. Thus, a strong sediment accumulation over the downstream small cylinder is observed, which contributed for the reduced S/D compared with that for the single cylinder case at $t = 45$ s. At this time instance, the flow is only strong enough to wash the sediments beneath the cylinders for the single cylinder and $G/D = 0$ cases. However, the jet flow and the vorticity next to the downstream cylinder are not strong enough to remove significant amounts of sediment for the $G/D = 0$ case due to the low θ. As a result, there is a very small gap where the jet flow escapes and consequently S/D is lower compared to the other cases.

Fig. 10 displays the streamlines for $\theta = 0.18$. At $t = 0.5$ s, the vortices attached to the main cylinder are suppressed for $G/D = 0$ and 0.15 compared with the other cases. The recirculation motion behind the sand dune at $t = 0.5$ s and 4.5 s close to the pipe in the single cylinder case occurs further downstream than the same for $\theta = 0.068$ shown in Fig. 9. With the development of scour, a recirculation motion is observed attached to the back face of the downstream cylinder for all the piggyback cases at $t = 4.5$ s. However, the gap flow beneath the piggyback and the vorticity are not strong enough to wash the sediments around them for $G/D = 0.15$, 0.25 and 0.35. Consequently, the gap flow escapes in between the main and the downstream cylinders and S/D can not develop as in the single cylinder and $G/D = 0$ cases. In contrast, the vortices in these cases are strong enough to transport the sediments around the cylinders far away, resulting in higher values of S/D as observed at $t = 45$ s.

The streamlines of the flow for the $\theta = 0.33$ are shown in Fig. 11. Compared with those for $\theta = 0.068$ and 0.18, the largest recirculation

behind the single cylinder moves to a location further downstream at $t =$ 0.5 s and 4.5 s. The stronger flow compared with those for $\theta = 0.068$ and 0.18 shown in Figs. 9 and 10, respectively, is sufficient to carry away all the sediments around the downstream cylinder for the $G/D = 0$, 0.15 and 0.35 configurations, resulting in high values of S/D. Nevertheless, for $G/D = 0.25$, the recirculation vortices behind the downstream cylinder are not strong enough to carry away the sediments around it, resulting in a significant deposition of sand over its surface. This strong blockage of the downstream pipeline causes the gap flow going through the opening between the main cylinder and the downstream cylinder, which further significantly reduces the development of S/D.

Therefore, in addition to the pressure gradient mechanism, the vortices around the cylinders also contribute significantly to the development of scour. If the vorticity close to the surface of the cylinders and the gap flow beneath them are strong enough to completely transport the sediments far away from the pipelines, large values of S/D are obtained. These results are consistent with the observations made by Mao (1986), Sumer and Fredsøe (1991) and Sumer et al. (2001) for the onset of scour.

5. Conclusion

In the present paper, numerical simulations are performed to investigate the scour beneath different setups of piggyback pipelines subjected to current flow. The two-phase flow numerical model developed by Cheng et al. (2017) known as SedFoam is employed. Convergence studies are carried out based on the time-history of the scour depth beneath the pipeline and the bed profile. A good agreement is achieved when the scour depth for different Shields parameters θ using the two-phase $k-\varepsilon$ model is compared to Mao (1986) experimental data. Single cylinder cases and multi-cylinders configurations are simulated for different values of θ. The most important findings based on the development of S/D and the bed profile are given as follows:

1. The scour development occurs faster in the earlier stages compared with the posterior ones.
2. In general, high values of θ result in high values of S/D.
3. The additional cylinders tend to contribute to reduce the maximum S/D and the accumulation of sediments at the back face of the downstream cylinder resulted in significant lower S/D.
4. As θ increases, the critical G/D, corresponding to the minimum development of the scour depth, increases.

The main conclusions based on the pressure gradient mechanism for the development of scour are:

1. The increase of θ results in higher values for the pressure gradient for all the geometries analyzed.
2. The maximum S/D is not strictly guided by the pressure gradient, as the development of scour changes the pattern of the flow significantly when additional cylinders are employed.

The major findings based on the vorticity mechanism for the development of scour are:

1. With the increase of θ, the stronger recirculation motion close to the back face of the pipe for the single cylinder cases takes place further downstream, which explains why the critical G/D increases as θ increases.
2. The capacity of the vortices and the jet flow to wash away the sediments around the downstream cylinder is a key factor for the development of scour. Otherwise, the jet flow beneath the pipeline will be guided through the gap between the main cylinder and the downstream cylinder, reducing the maximum S/D.

CRediT authorship contribution statement

Vinicius Serta Fraga: Conceptualization, Methodology, Software, Validation, Formal analysis, Investigation, Writing – original draft, Writing – review & editing, Visualization. **Guang Yin:** Conceptualization, Methodology, Software, Validation, Formal analysis, Investigation, Writing – original draft, Writing – review & editing, Visualization. **Muk Chen Ong:** Conceptualization, Investigation, Formal analysis, Writing – review & editing, Resources, Supervision. **Dag Myrhaug:** Conceptualization, Investigation, Writing – review & editing.

Declaration of competing interest

The authors declare that they have no known competing financial interests or personal relationships that could have appeared to influence the work reported in this paper.

Acknowledgement

This study is supported with computational resources provided by the Norwegian Metacenter for Computational Science (NOTUR), under Project No: NN9372K.

References

Brørs, B., 1999. Numerical modeling of flow and scour at pipelines. J. Hydraul. Eng. 125, 511–523. https://doi.org/10.1061/(ASCE)0733-9429(1999)125:5(511).

Chauchat, J., Cheng, Z., Nagel, T., Bonamy, C., Hsu, T.-J., 2017. SedFoam-2.0: a 3D two-phase flow numerical model for sediment transport. Geosci. Model Dev. Discuss. (GMDD) 1–42. https://doi.org/10.5194/gmd-2017-101.

Cheng, Z., Hsu, T.-J., 2014. A Multi-Dimensional Two-phase Eulerian Model for Sediment Transport - twoPhaseEulerSedFoam (Version 1.0). CACR-14-08, Center for Applied Coastal Research, University of Delaware.

Cheng, Z., Hsu, T.-J., Calantoni, J., 2017. SedFoam: a multi-dimensional Eulerian two-phase model for sediment transport and its application to momentary bed failure. Coast. Eng. 119, 32–50. https://doi.org/10.1016/j.coastaleng.2016.08.007.

Chiew, Y.-M., 1992. Effect of spoilers on scour at submarine pipelines. J. Hydraul. Eng. 118 https://doi.org/10.1061/(ASCE)0733-9429(1992)118:9(1311).

Ding, J., Gidaspow, D., 1990. A bubbling fluidization model using kinetic theory of granular flow. AIChE J. 36 (4), 523–538.

Guo, Z., Jeng, D.-S., Zhao, H., Guo, W., Wang, L., 2018. Effect of seepage flow on sediment incipient motion around a free spanning pipeline. Coast. Eng. 143 https://doi.org/10.1016/j.coastaleng.2018.10.012.

Jakobsen, M.L., Sayer, P., 1995. Hydrodynamic forces on piggyback pipelines. In: The 5th International Offshore and Polar Engineering Conference, Hague, Netherlands, vol. 1, pp. 139–147.

Larsen, B., Fuhrman, D., Sumer, B., 2016. Simulation of wave-plus-current scour beneath submarine pipelines. J. Waterw. Port, Coast. Ocean Eng. 142, 04016003 https://doi.org/10.1061/(ASCE)WW.1943-5460.0000338.

Lasatira, G., Suntoyo, S., Armono, H., 2017. Numerical model for prediction the scour depth around two pipelines in tandem. Appl. Mech. Mater. 862, 332–337. https://doi.org/10.4028/www.scientific.net/AMM.862.332.

Lee, C.-H., Low, Y., Chiew, Y.-M., 2016. Multi-dimensional rheology-based two-phase model for sediment transport and applications to sheet flow and pipeline scour. Phys. Fluids 28, 053305. https://doi.org/10.1063/1.4948987.

Li, Y., Ong, M.C., Fuhrman, D., Larsen, B., 2019a. Numerical investigation of wave-plus-current induced scour beneath two submarine pipelines in tandem. Coast. Eng. 156 https://doi.org/10.1016/j.coastaleng.2019.103619.

Li, Y., Ong, M.C., Fuhrman, D., 2019b. CFD investigations of scour beneath a submarine pipeline with the effect of upward seepage. Coast. Eng. 156, 103624. https://doi.org/10.1016/j.coastaleng.2019.103624.

Mao, Y., 1986. The Interaction between a Pipeline and an Erodible Bed. Institute of Hydrodynamics and Hydraulic Engineering Københavns: Series Paper; Institute of Hydrodynamics and Hydraulic Engineering, Technical University of Denmark, Lyngby, Denmark.

Mathieu, A., Chauchat, J., Bonamy, C., Nagel, T., 2019. Two-phase flow simulation of tunnel and lee-wake erosion of scour below a submarine pipeline. Water. https://doi.org/10.3390/w11081727, 11. 1727.

Nagel, T., Chauchat, J., Bonamy, C., Liu, X., Cheng, Z., Hsu, T.-J., 2020. Three-dimensional scour simulations with a two-phase flow model. Adv. Water Resour. 103544 https://doi.org/10.1016/j.advwatres.2020.103544.

Qi, W.-G., Gao, F.-P., 2014. Physical modeling of local scour development around a large-diameter monopile in combined waves and current. Coast. Eng. 83, 72–81. https://doi.org/10.1016/j.coastaleng.2013.10.007.

Soulsby, R., 1997. Dynamics of Marine Sands. Thomas Telford, UK.

Sumer, B., Fredsoe, Jorgen, 1991. Onset of scour below a pipeline exposed to waves. In: Int. J. Offshore Polar Engineering Conference, 1, pp. 189–194.

Sumer, B., Mao, Ye, Fredsøe, J., 1988. Interaction between vibrating pipe and erodible bed. J. Waterw. Port, Coast. Ocean Eng. https://doi.org/10.1061/(ASCE)0733-950X(1988)114:1(81).

Sumer, B., Truelsen, C., Sichmann, T., Fredsoe, J., 2001. Onset of scour below pipelines and self-burial. Coast. Eng. 42, 313–335. https://doi.org/10.1016/S0378-3839(00)00066-1.

Wilcox, D., 2006. Turbulence Modeling for CFD, third ed. DCW industries La Canada, CA.

Wilcox, D., 2008. Formulation of the k-omega turbulence model revisited. AIAA J. 46 (11), 2823–2838.

Yang, S., Shi, B., Guo, Y., Yang, L., 2019. Investigation on scour protection of submarine piggyback pipeline. Ocean Eng. 182, 442–450. https://doi.org/10.1016/j.oceaneng.2019.04.090.

Zhai, H., Jeng, D.-S., Guo, Z., 2021a. The role of 2D seepage on sediment incipient motion around a pipeline. J. Mar. Sci. Eng. 9, 580. https://doi.org/10.3390/jmse9060580.

Zhai, H., Jeng, D.-S., Guo, Z., Liang, Z., 2021b. Impact of two-dimensional seepage flow on sediment incipient motion under waves. Appl. Ocean Res. 108, 102510. https://doi.org/10.1016/j.apor.2020.102510.

Zhao, E., Shi, B., Qu, K., Dong, W., Zhang, J., 2018. Experimental and numerical investigation of local scour around submarine piggyback pipeline under steady current. J. Ocean Univ. China 17, 244–256. https://doi.org/10.1007/s11802-018-3290-7.

Zhao, M., Cheng, L., 2008. Numerical modeling of local scour below a piggyback pipeline in currents. J. Hydraul. Eng. 134 (10).

Zhao, L., Guo, B., Bai, X., Zhang, W., Li, T., Williams, J.J.R., 2016. Finite element modelling of local scour below a pipeline under steady currents. Int. J. Comput. Fluid Dynam. 30, 1–6. https://doi.org/10.1080/10618562.2016.1142076.

Zhu, H., Qi, X., Lin, P., Yang, Y., 2013. Numerical simulation of flow around a submarine pipe with a spoiler and current-induced scour beneath the pipe. Appl. Ocean Res. 41, 87–100. https://doi.org/10.1016/j.apor.2013.03.005.